Biomimetic Design and CFD-Based Optimization of an Underwater ROV: Hydrodynamic Analysis and Manufacturing Constraints

Moemen M. Adel[1*], Abdallah Hany Alsaid[1], Ahmed Nasser[2], Ahmed Mekki[1], Ahmed M. Fouad[1], Mahmoud G. Abdelfateh[1], Ahmed M. Hanafi[1], Ahmed E. Newir[1]

[1] Department of Mechatronics Engineering, Faculty of Engineering, October 6 University, 6th of October City, 12585, Giza, Egypt.
[2] Department of Basic Sciences, Faculty of Engineering, October 6 University, 6th of October City, 12585, Giza, Egypt.
* Corresponding author's email: moemen.mohamed.eng@o6u.edu.eg

Abstract:
This study presents a comprehensive Computational Fluid Dynamics (CFD) investigation to optimize the hydrodynamic performance of a Remotely Operated Vehicle (ROV) designed for underwater applications. Inspired by the morphology of the ray fish, three design iterations were analyzed—initial, biomimetic, and manufacturable-final—to assess thrust generation, drag force, pressure distribution, and velocity streamlines across various flow regimes. Using ANSYS CFD and the SST k-ω turbulence model, each configuration was tested at velocities ranging from 0.5 m/s to 10 m/s. Results demonstrated a progressive reduction in drag force from 25.85 N in the initial design to 14.13 N in the final model at 1 m/s, alongside a pressure drop from 550 Pa to 400 Pa. The final biomimetic design, divided into modular sections for ease of manufacturing, achieved an optimal balance between performance and constructability. Moreover, the dome-shaped front improved high-speed fluid dynamics but was substituted with a flat face due to fabrication challenges. Pressure contour and streamline analysis confirmed enhanced stability and reduced turbulence in the final design. This work highlights the critical role of CFD in the hydrodynamic refinement of ROVs and demonstrates how biomimicry and engineering pragmatism can converge to yield efficient and feasible underwater systems.

Keywords:
Remotely Operated Vehicle (ROV), Computational Fluid Dynamics (CFD), Hydrodynamic Optimization, Biomimicry, Thrust and Drag Analysis, Underwater Robotics

1   Introduction

The increasing demand for oil and gas exploration in deep-water environments necessitates advanced technologies to ensure safety, efficiency, and precision. Remotely Operated Vehicles (ROVs) play a critical role in underwater inspections, maintenance, and repairs, but their performance hinges on optimal hydrodynamic design. This study leverages Computational Fluid Dynamics (CFD) to enhance the ROV's thrust, stability, and maneuverability by analyzing fluid-structure interactions under varying operational conditions.

The concept of biomimicry learning from and emulating nature's time-tested patterns and strategies has proven highly effective in engineering design, particularly in optimizing hydrodynamic performance. In this study, ray fish morphology was selected as a biological inspiration due to its naturally efficient movement through aquatic environments, which aligns well with the objectives of reducing drag force and enhancing stability in Remotely Operated Vehicles (ROVs) [1].

1.1   Previous Research

This research focuses on improving the hydrodynamic performance of a newly developed Remotely Operated Vehicle (ROV) of the Observation Class using Computational Fluid Dynamics (CFD) simulations. The study aimed to optimize the ROV's design to reduce drag and enhance underwater movement efficiency. The methodology involved creating a 3D model, generating a mesh and computational domain, and simulating fluid flow under different motion conditions, including horizontal translation and diving with varying angles. Results showed a significant improvement in the hydrodynamic characteristics of the optimized design, with a 43% reduction in drag coefficient compared to the previous model. Although no explicit future work is mentioned, the study implies potential for further design refinement and real-world testing.[2]

Steinar Skorpa investigated the hydrodynamic behavior around a Remotely Operated Vehicle (ROV), specifically the Merlin WR200, using Computational Fluid Dynamics (CFD) simulations with the Detached Eddy Simulation (DES) approach and the k–ω SST turbulence model. The study began with simulations on simplified cube models to validate methodology, revealing that rounded edges significantly reduce drag compared to sharp ones. Subsequently, a simplified ROV model was analyzed, showing small grid convergence variations and revealing instability caused by pressure differences around the vehicle's body particularly in the regions above the front top and below the aft bottom. A consistent negative pitch moment confirmed the vehicle's instability in survey mode. As future work, the study recommends running simulations without the rear plate and repositioning components located in front of it to assess their influence on flow behavior and improve overall stability.[3]

Oskar Voldsund focused on estimating and validating the hydrodynamic parameter specifically added mass and damping—of the Merlin UCV work-class ROV using Computational Fluid Dynamics (CFD) simulations in Open FOAM. The objective is to improve the realism and accuracy of a simulator used for training and technology testing by replacing previously intuitive parameter estimation methods with systematic CFD-based modeling. Various CFD simulations, including towing tank, rotating arm, and planar motion mechanism (PMM) tests, were carried out to estimate damping and added mass in all six degrees of freedom. These results were then validated by comparing them with recorded operational data from a real ROV at Snorre B (SNB), achieving good alignment. Adjusting the CFD-derived parameters to better fit real-world data led to improved simulation accuracy. The thesis concludes that while CFD is a powerful standalone method for estimating hydrodynamic parameters, combining it with recorded data yields more accurate and efficient results. Future work suggests using this approach for developing digital twins of ROVs to facilitate design and operation optimization [4].

Another study optimized the thrust and maneuverability of a Remotely Operated Vehicle (ROV) by investigating different thruster configurations using Computational Fluid Dynamics (CFD). The research was motivated by the need to enhance the ROV's performance for competitive robotics events, focusing on variations in propeller blade count (2, 3, and 4 blades) and the application of a Kort nozzle. Simulations using ANSYS CFX revealed that the Kort nozzle improved thrust by accelerating fluid flow and reducing turbulence, with the 3-blade propeller (P3-2020) paired with a Kort nozzle achieving the highest thrust increase (2.253%) and a 21.053% reduction in turbulent flow. Future work suggests exploring larger propellers (e.g., 4-blade designs) pending manufacturing feasibility.

Chin et al. explored computational methods using CFD (STAR-CCM+) and potential flow analysis (WAMIT) to model complex-shaped ROVs. They validated these models through experimental tests in a controlled water tank, specifically analyzing heave and yaw motions. Their work demonstrated that simulation-based approaches can effectively substitute costly physical testing in early design stages.[5]

J. A. Ramírez-Macías focused on developing a hydrodynamic model for the inspection-class ROV Visor3 using Computational Fluid Dynamics (CFD) to predict maneuvering coefficients for control system design. The research employed the viscous-flow solver ReFRESCO to simulate forces and moments under various scenarios, including steady-state inflow angle variations, circular maneuvers, and unsteady rotations. Key steps included simplifying the ROV geometry, conducting Virtual Captive Tests (VCT), and fitting CFD data to Taylor-series-like polynomial models to quantify hydrodynamic effects. Results revealed that while force models fit well, moment models required highly nonlinear terms for accuracy. The study concluded with a set of validated maneuvering coefficients (e.g., drag and coupling terms) but highlighted the need for experimental validation, further unsteady flow analysis, and tether influence studies. Future work aims to refine the model for advanced control systems and address limitations in moment predictions [6].

1.2   Buoyancy and Stability

Any vehicle has movement about six degrees of freedom Figure 1: three translations (surge, heave, and sway along the longitudinal, vertical, and transverse (lateral) axes, respectively) and three rotations (roll, yaw, and pitch about these same respective axes), this section will address the interaction between vehicle static and dynamic stability and these degrees of freedom.[7]
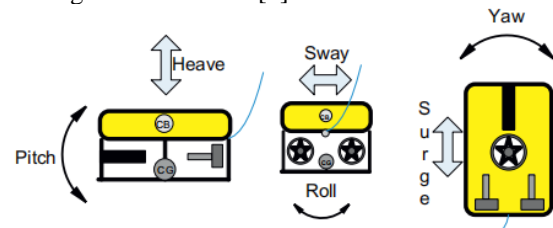

Figure 1: Degrees of Freedom of an ROV in 3D Space.

ROVs are not normally equipped to pitch and roll. The system is constructed with a high center of buoyancy and a low CG to give the camera maximum stability about the longitudinal and lateral axes Figure 2. Most ROV systems have fixed ballast with variable positioning to allow trimming of the system nose-up/nose-down or for roll adjustment/trim. In the observation class, the lead (or heavy metal) ballast is normally located on tracks attached to the bottom frame to allow movement of ballast along the vehicle to achieve the desired trim.[7]

Aguirre-Castro et al. investigated the design and construction of a low-cost, Raspberry Pi 3–based ROV for underwater exploration. They integrated a smart PID controller with a complementary filter to improve motor stability and image quality. Their ROV achieved real-time video capture of up to 42 FPS and could operate up to 100 meters underwater. Parallel processing, open-source tools, and modular design enhanced the system's flexibility for marine applications.[8]
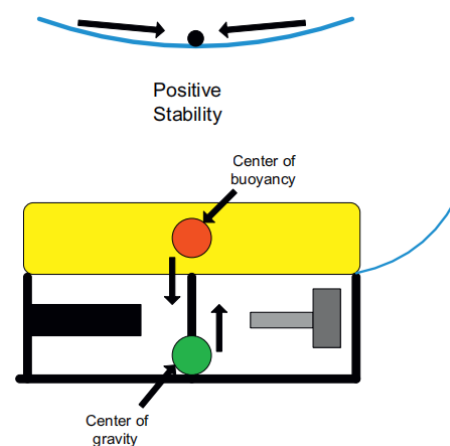

Figure 2: ROV Stability Configuration with High Buoyancy Center

According to Archimedes' principle, anybody partially or totally immersed in a fluid is buoyed up by a force equal to the weight of the displaced fluid. If somehow one could remove the body and instantly fill the resulting cavity with fluid identical to that surrounding it, no motion would take place: The body weight would exactly equal that of the displaced fluid. The result of all the weight forces on this

displaced fluid Figure 3 is centered at a point within the body termed the "center of gravity" (CG) Figure 4.[7]
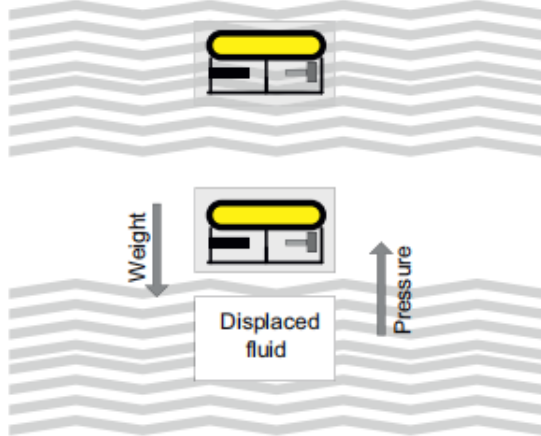

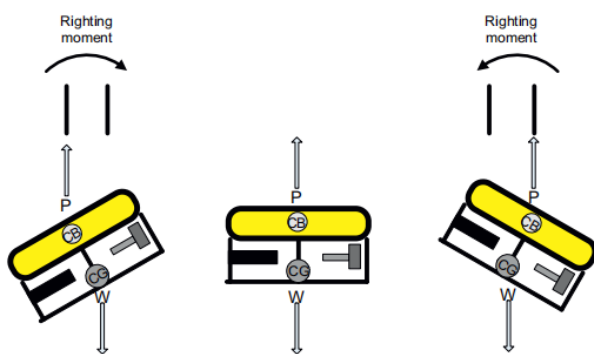**Figure 3: Illustration of Hydrostatic Equilibrium in Fluid**

Figure 4: Righting Moment Concept in ROV Design

The objective of this study is to design, simulate, and optimize a biomimetic Remotely Operated Vehicle (ROV) using Computational Fluid Dynamics (CFD). The study focuses on evaluating multiple ROV configurations to enhance hydrodynamic performance by analyzing thrust efficiency, pressure distribution, and drag forces across varying flow velocities. Through detailed CFD simulations, the research aims to reduce turbulence and improve energy efficiency. The goal is to develop an accurate and realistic virtual model suitable for simulation-based training and control system development.[7]

2   Methods

The design methodology adopted in this study follows a structured and iterative process, as illustrated in the methodological flowchart Figure 5.The process begins with an extensive review of previous research on Remotely Operated Vehicles (ROVs), focusing on hydrodynamic performance, buoyancy principles, and stability considerations. Based on insights from the literature, a preliminary model of the ROV was developed using computer-aided design (CAD) software. The initial model incorporated basic thruster arrangements and structural geometry, which were then subjected to Computational Fluid Dynamics (CFD) analysis to evaluate hydrodynamic performance, including thrust efficiency, pressure distribution, and flow behavior. If the model did not meet performance expectations, it was redesigned using a biomimetic approach—drawing inspiration from the

streamlined shape of a ray fish to enhance flow characteristics and minimize drag. This revised design was compared against other configurations to identify the optimal solution in terms of performance and manufacturability. The most suitable design underwent further CFD analysis at multiple flow velocities ranging from 0.5 m/s to 10 m/s to observe its response under varying conditions. Finally, detailed pressure distribution studies were conducted on the refined model to assess structural loading and confirm hydrodynamic efficiency. This methodological framework integrates engineering analysis with nature-inspired design principles to develop a high-performance and manufacturable ROV configuration.
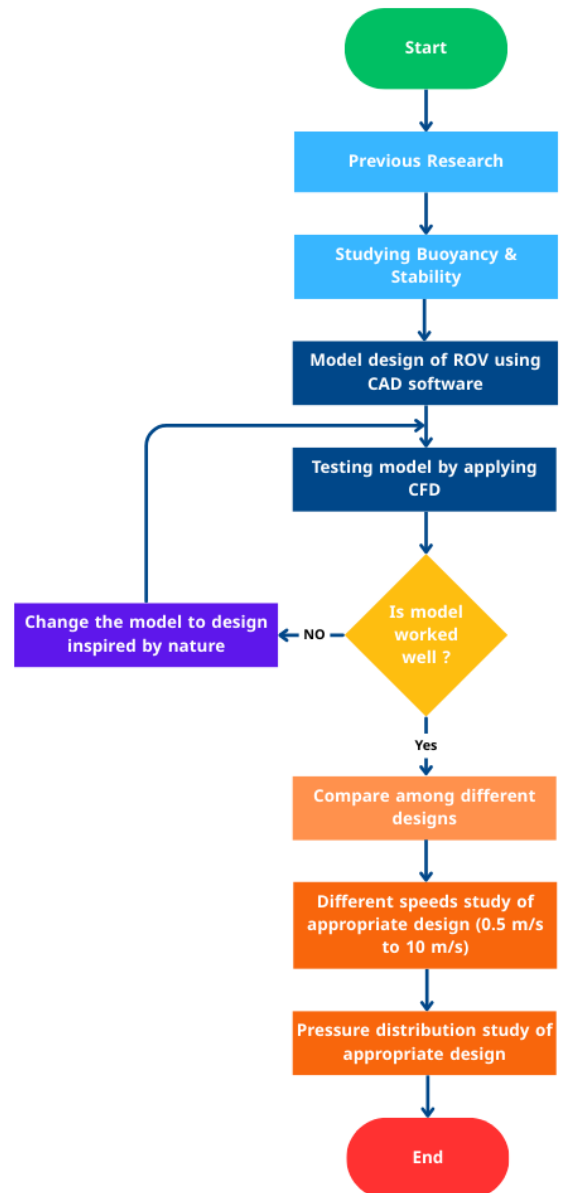

Figure 5: Methodological Flowchart for Biomimetic ROV Design and Hydrodynamic Evaluation

From results taken from ANSYS, it was found that drag force equals 25.865 newtons at velocity equals to 1 m/s, so from drag force equation (1):

The drag force acting on the ROV can be estimated using the standard fluid dynamics equation

$$F_d = \frac{1}{2} \rho v^2 c_d A \qquad (1)$$

Where:

- F_d is the drag force (N),
- ρ is the fluid density (kg/m³),
- V is the velocity of the fluid relative to the body (m/s),
- c_d is the drag coefficient (dimensionless),
- A is the reference area or the frontal area of the body facing the flow (m²).

The static pressure distribution over the surface of laboratory glider in terms of pressure coefficient (Cp) whose definition is[9]

$$P_t = 0.5\, C_P\, \rho\, V^2 \tag{2}$$

Where:

P_t represents the total pressure at any orientation.

Froude and Reynolds numbers can be estimated using the following equation.[10]

$$F_r = \frac{V}{\sqrt{gl}} \tag{3}$$

$$R_e = \frac{\rho\, V\, l}{\mu} \tag{4}$$

Where:

- g is gravitational acceleration,
- l is characteristic length,
- μ is the viscosity.

In this study, the hydrodynamic performance of ROV is evaluated by CFD. The fluid motion around the ROV is simulated by solving the Reynolds Average Navier-Stokes (RANS) equations, including the continuity equation and the momentum equation [11], [12], [13], [14], [15].

$$\rho \frac{\partial u_i}{\partial t} + \rho \frac{\partial u_i\, u_j}{\partial x_j} = -\frac{\partial p}{\partial x_i} + \rho g_i$$
$$+ \rho \frac{\partial}{\partial x_j}\left[\mu\left(\frac{\partial u_i}{\partial x_j} + \frac{\partial u_j}{\partial x_i}\right) \right. \tag{5}$$
$$\left. - \overline{u_i' u_j'} \right]$$

Where:

- t is the physical time and
- $-\rho\, \overline{u_i' u_j'}$ is the Reynolds stress

The governing equations consist of mass and momentum conservation equations with a shear stress transport (SST) k-ω turbulence model for the three-dimensional, incompressible Newtonian fluid flow are as follows:[16]

$$-\rho\, \overline{u_i' u_j'} = \mu_t \left(\frac{\partial u_i}{\partial x_j} + \frac{\partial u_j}{\partial x_i}\right) - \frac{2}{3}\rho\, k_t\, \delta_{ij} \tag{6}$$

$$\frac{\partial (\rho\, k_t)}{\partial t} + \frac{\partial (\rho\, k_t\, u_i)}{\partial x_i}$$
$$= \frac{\partial}{\partial x_j}\left[\left(\mu + \frac{\mu_t}{\sigma_k}\right)\frac{\partial k_t}{\partial x_j}\right] + \tilde{P}_k \tag{7}$$
$$- \beta^* \rho\, k_t\, \omega$$

$$\frac{\partial (\rho\, \omega)}{\partial t} + \frac{\partial (\rho\, \omega u_i)}{\partial x_i}$$
$$= \frac{\partial}{\partial x_j}\left[\left(\mu + \frac{\mu_t}{\sigma_\omega}\right)\frac{\partial \omega}{\partial x_j}\right] + P_\omega \tag{8}$$
$$- \beta\, \rho\, \omega^2$$
$$+ 2\rho(1 - F_1)\, \frac{1}{\sigma_{\omega^2}\omega}\, \frac{\partial k_t}{\partial x_j}\, \frac{\partial \omega}{\partial x_j}$$

$$\tilde{P}_k = \min(P_k\,,\, 10\, \beta^*\, \rho\, k_t\, \omega) \tag{9}$$

$$P_k = 2\mu_t\, S_{ij}.S_{ij} - \frac{2}{3}\rho\, k_t\, \frac{\partial u_i}{\partial x_j}\, \delta_{ij} \tag{10}$$

$$P_\omega = \gamma\left(2\rho\, S_{ij}.S_{ij} - \frac{2}{3}\rho\, \omega\, \frac{\partial u_i}{\partial x_j}\, \delta_{ij}\right) \tag{11}$$

Where:

- μ_t is the turbulent eddy viscosity,
- k_t is turbulent kinetic energy,
- δ_{ij} is the Kronecker delta function.
- $\tilde{P}_k$ is the effective rate,
- P_k is the production rate of turbulent kinetic energy,
- P_ω is the rate of production of specific dissipation rate,
- S_{ij} is the mean rate of deformation components, and
- σ_ω, β and γ are the SST k-ω model constants.

To achieve optimal hydrodynamic performance, multiple ROV design configurations were developed and evaluated. The initial design featured a total of six thrusters—two oriented horizontally and four vertically—to ensure maneuverability across all degrees of freedom. The structure also incorporated a central hollow cylindrical compartment intended to house electronic components, enabling compact integration of control systems and sensors as shown in Figure 6.
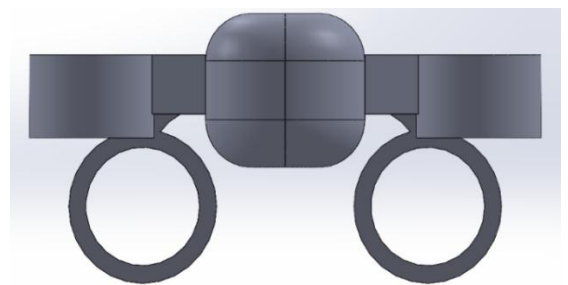
Design 1 Front View
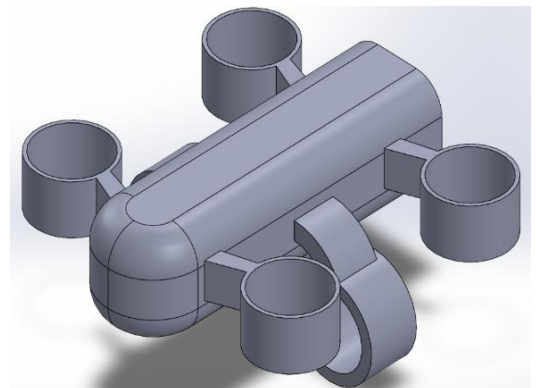
Design 1 Isometric View

Figure 6: CAD Layout of Initial ROV Design (Front and 3D Views)

Another design was developed based on the morphology of a ray fish, aiming to enhance hydrodynamic efficiency while improving the mass distribution and overall volume of the ROV. This biomimetic approach was intended to reduce drag, promote smoother fluid flow around the body, and achieve greater stability during underwater operation as shown in
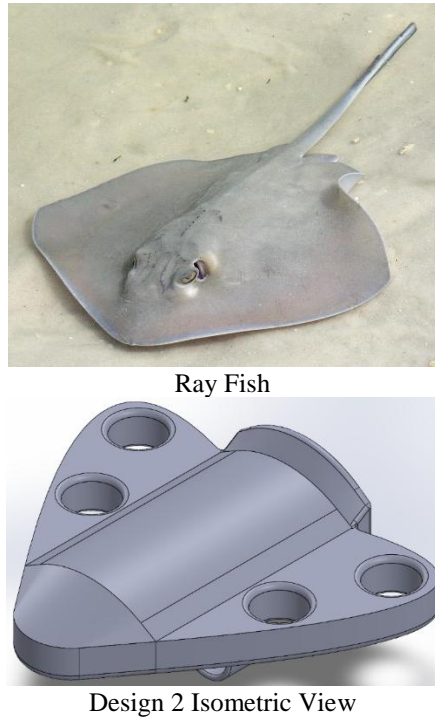
Figure 7.

Ray Fish

Design 2 Isometric View

Figure 7: Biomimetic ROV Design Inspired by Ray Fish (CAD and Natural Reference).

Figure 6 and

Figure 7 illustrates the two designs used in the research. The study analyzed the results of the two designs to determine which design will meet the objectives. Figure 6 shows the design that has been inspired by the real ray fish as it can reach the bottom of the ocean without any problem.

CFD is employed in this research because it offers a powerful and systematic approach for predicting complex fluid-structure interactions without the need for extensive and expensive experimental testing. By numerically solving the Navier–Stokes equations, CFD provides detailed insights into the forces acting on the ROV in various flow conditions. Unlike traditional empirical or pilot-feedback-based methods, CFD enables the estimation of hydrodynamic coefficients with high spatial and temporal resolution, thus enhancing the reliability and performance of ROV simulators and enabling the development of digital twins for underwater applications.

o ANSYS CFD was employed to simulate fluid flow around the ROV at speeds of 0.5–10 m/s, using the SST k-ω turbulence model for accurate boundary layer predictions.

o Key analysis included:

- Pressure distribution on the ROV surface to identify stress concentrations.
- Velocity streamlines to assess flow separation and vortex formation.

- Drag/thrust force calculations to optimize propulsion efficiency.

3   Results and Discussion

Figure 8 show two charts represent the thrust force (in Newtons) as a function of velocity (in meters per second) for two different propulsion system designs. Upon examining the overall trend of both graphs, it is immediately evident that both thrust profiles are nonlinear, exhibiting a sharp increase in force as velocity increases. However, the rate and shape of that increase differ significantly between the two.
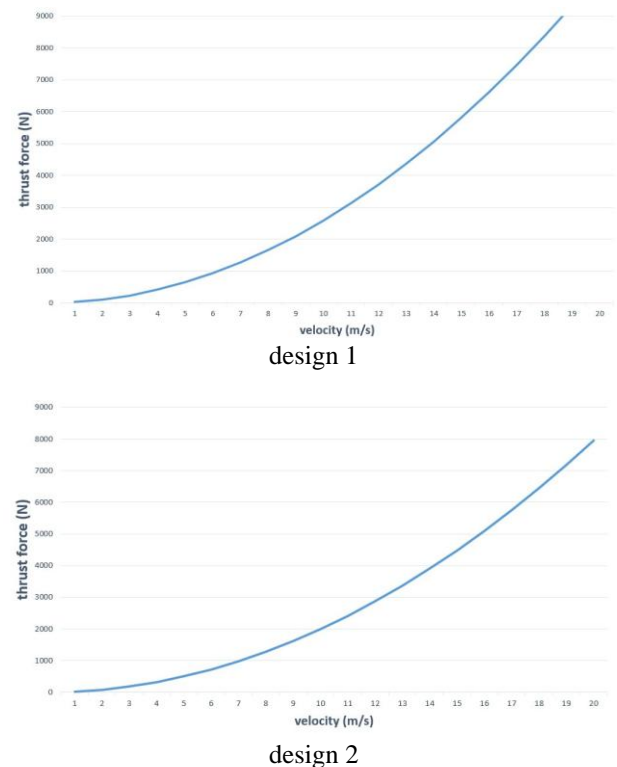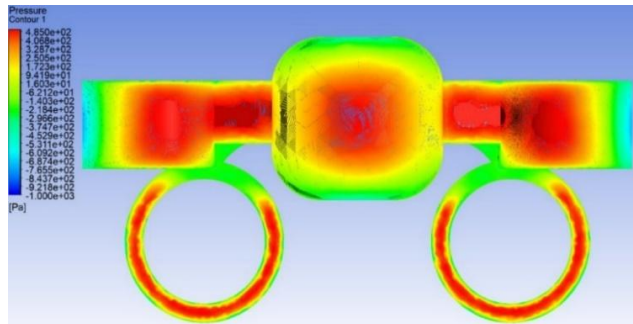
design 1

design 2

Figure 8: Thrust Force versus Velocity for Design 1 and Design 2

In Design 1, the thrust force starts relatively low at lower velocities but climbs much more steeply as velocity increases. The curve shows an accelerated growth, typical of a quadratic or higher-order polynomial relationship, suggesting that thrust increases at a faster rate than velocity itself. This design achieves a peak thrust of approximately 9000 N at 20 m/s, showcasing its strength in high-velocity environments. Such a profile would be well-suited for applications where rapid acceleration and powerful high-speed performance are crucial, such as in supersonic drones, underwater torpedoes, or high-thrust aerospace systems.

Conversely, Design 2 exhibits a more gradual increase in thrust with velocity. Although it also follows a nonlinear trend, the curve rises more smoothly and less aggressively compared to Design 1. At 20 m/s, it reaches a maximum thrust of about 8000 N, which is 1000 N less than Design 1 at the same speed. Interestingly, Design 2 appears to offer slightly higher thrust at lower velocities, particularly in the range from 1 to 10 m/s, which may indicate better low speed efficiency. This would make Design 2 ideal for systems that require consistent and efficient thrust at sub-maximal speeds, such as electric UAVs, hybrid vehicles, or energy-conservative marine systems. From an engineering perspective, the key trade-off between these two designs lies in their performance across different velocity regimes.

Design 1 offers superior thrust at higher speeds, which could come at the cost of greater energy consumption or increased mechanical stress. Meanwhile, Design 2 maintains a more balanced output, sacrificing peak performance for improved consistency and potentially better energy efficiency at lower speeds.

In conclusion, Design 1 is optimized for peak performance and aggressive acceleration, while Design 2 favors smooth operation and early velocity efficiency. Selecting between them would depend on the mission requirements—whether the application demands top-speed dominance or balanced thrust across a broader range.

Design 1 pressure distribution
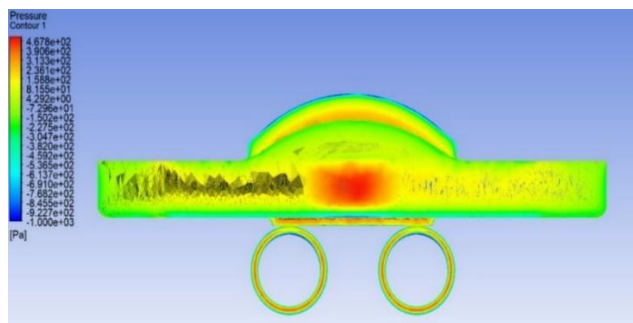
Design 2 pressure distribution

Figure 9: Pressure Distribution Contours on Initial and Biomimetic ROV Designs

Figure 9 is a computational fluid dynamic (CFD) pressure contour map, revealing the pressure distribution over a dual-ringed aerodynamic or hydrodynamic structure—likely a component of a propulsion system for design 1. The color map on the left indicates pressure values in Pascals (Pa), ranging from a maximum of approximately +485 Pa (represented by red zones) down to a minimum of around -1100 Pa (depicted by dark blue). This broad range signifies substantial pressure differentials across the surface, which are crucial for understanding both aerodynamic loading and flow behavior.

The central body of the structure is heavily saturated with red coloring, indicating a region of high pressure. This is characteristic of a stagnation zone where the incoming fluid (air or water) directly impacts the surface and loses velocity, thereby converting kinetic energy into pressure. This pressure accumulation is a key driver of drag and suggests that the central housing is bearing the brunt of frontal aerodynamic or hydrodynamic resistance. From an engineering standpoint, this may represent an opportunity to streamline the central housing to reduce pressure build-up and, consequently, the overall drag force.

Moving outward from the center, the arms that connect the central body to the dual rings also display notable pressure increases, particularly around their joints and transitions. This suggests flow constriction and possible vortex formation due to abrupt changes in geometry. These pressure buildups could contribute to local drag and also introduce mechanical stress points that need to be considered during structural design.

The two large rings exhibit distinctive high-pressure zones along their outer edges, forming clear red outlines. This indicates that significant pressure forces are concentrated around the ring peripheries, likely due to interaction with internal propulsion components like rotors or fans. The inner portions of the rings, transitioning into green and blue, show lower pressure regions, which are consistent with areas of accelerated flow or suction..

Finally, the rear and lower portions of the geometry exhibit cooler tones—green, cyan, and blue—which correspond to lower pressures and possible flow detachment zones. These are critical areas for assessing flow wake and turbulence, which can severely impact efficiency and stability. In particular, the blue zones near the rear hint at potential low-pressure wakes that could cause drag and vortex shedding.

Overall, this pressure map provides key insights into how the fluid interacts with the surface of the structure. The most intense aerodynamic or hydrodynamic loads appear concentrated on the central front and ring peripheries, indicating zones that would benefit from design refinement. Streamlining, curvature adjustments, or implementing flow-guiding vanes could help reduce drag, enhance thrust, and distribute stress more evenly across the structure.

In terms of pressure behavior for the second design, the second design likely exhibits lower peak pressure values at the front, implying a reduction in stagnation pressure due to improved flow guidance or reduced frontal area. The shape may also facilitate smoother acceleration of the fluid around the body, which would create more evenly distributed pressure gradients along the surface. This contributes to minimizing pressure drag, which is aligned with the observed performance difference in the thrust graph.

Additionally, the ring structures in the second design are expected to show less intense pressure spikes along their outer edges. This would be consistent with improved duct shaping or changes in the curvature that help reduce flow separation and turbulence. As a result, the high-pressure outlines that were visible in the first design's pressure plot would appear less pronounced or shifted slightly rearward in the second design.

Finally, the low-pressure wake zones—often a byproduct of abrupt geometry or bluff-body flow—are likely more controlled in the second design. If wake reduction features or aerodynamic fairings were introduced, these would help suppress large low-pressure areas that form behind the structure, improving efficiency and stability. Therefore, the second design's pressure distribution is expected to be more balanced, with reduced extremes and a smoother pressure gradient from front to back.
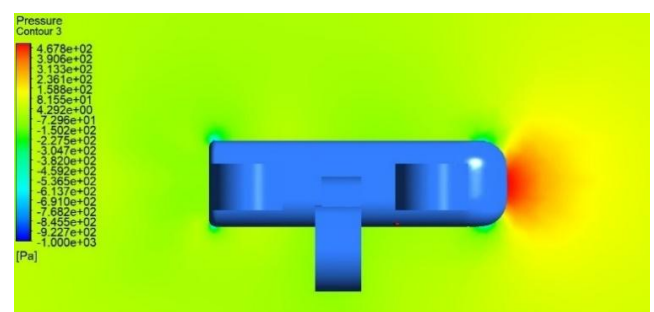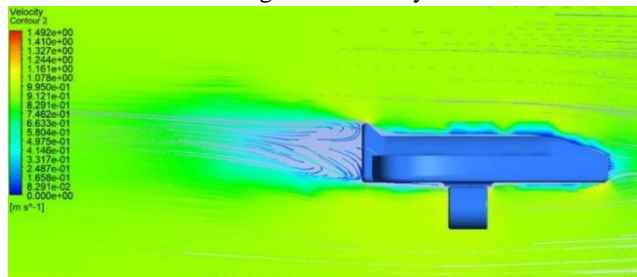

Design 1 Pressure concentration on the mid plane
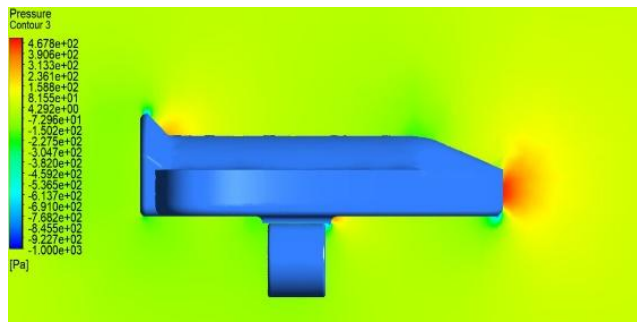
Design 2 Pressure concentration on the mid plane

Figure 10: Mid-Plane Pressure Distribution Comparison between Two ROV Designs
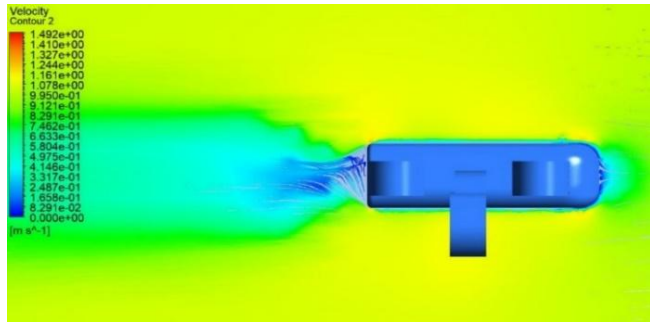
Design 1 flow study

Design 2 flow study

Figure 11: Streamline Velocity Flow Comparison of Initial and Biomimetic Designs.

Considering the practical constraints associated with manufacturing the proposed designs, it was determined that fabricating the original body structure of the biomimetic ROV would be both technically challenging and cost prohibitive. To address this, the second design—based on the ray fish morphology—was modified to enhance its manufacturability. As illustrated in Figure 13, the final design was restructured into modular components that can be fabricated individually and assembled using bolts. This approach not only reduced production complexity and cost but also facilitated easier maintenance and potential component replacement.

In line with the principles of biomimicry defined as the imitation of natural forms, processes, and systems, the wing structure of the ROV was carefully designed to emulate the morphology of a ray fish. This biologically inspired approach was adopted to enhance the vehicle's hydrodynamic performance by leveraging nature's optimized geometry for fluid flow. The resulting configuration was not only effective in improving flow characteristics but was also engineered

with attention to structural and mass distribution parameters. As presented in

Table 1, the final ROV assembly achieved a total mass of 10,021.61 grams, a volume of 8,393,636.26 cubic millimeters, and a surface area of 2,162,160.90 square millimeters. The center of mass was located at X = -0.21 mm, Y = 196.61 mm, and Z = -26.99 mm, confirming the design's balance and stability for underwater operation.

Table 1: Mass and Geometric Properties of Final ROV Assembly

Property	Value
Mass	10,021.61 grams
Total Weld Mass	0.00 grams
Volume	8,393,636.26 cubic millimeters
Surface Area	2,162,160.90 square millimeters
Center of Mass (X)	-0.21 mm
Center of Mass (Y)	196.61 mm
Center of Mass (Z)	-26.99 mm
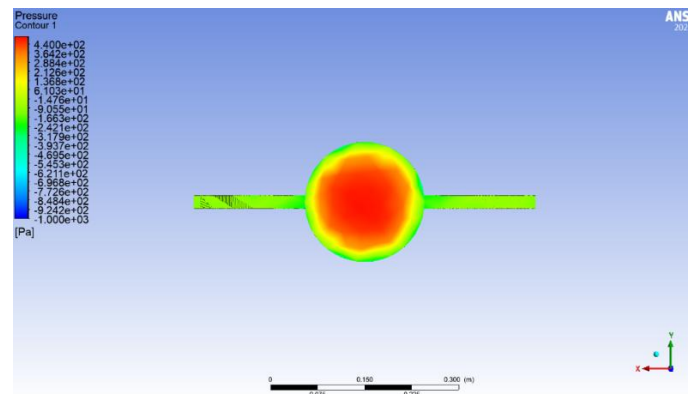
Figure 12: Pressure Contour of Final ROV Design at 1 m/s

At a flow velocity of 1 m/s, the pressure contour of the final ROV design reveals a distinct concentration of high-pressure regions on the frontal surface of the vehicle. As illustrated in Figure 13, the red zone at the center indicates a maximum pressure of approximately 440 Pa, corresponding to the stagnation point where the incoming fluid directly impacts the ROV body. Surrounding this central area, the pressure gradually decreases toward the periphery, forming a well-defined pressure gradient that transitions from red to green and eventually to blue, indicating regions of lower pressure. This distribution is consistent with expectations for a blunt-body flow profile, where the forward-facing geometry induces significant pressure buildup. The symmetrical nature of the pressure field confirms the balanced design of the ROV, while the uniform gradient along the lateral edges suggests efficient flow reattachment with minimal asymmetry. These findings support the hydrodynamic viability of the final design, particularly under moderate-speed conditions.
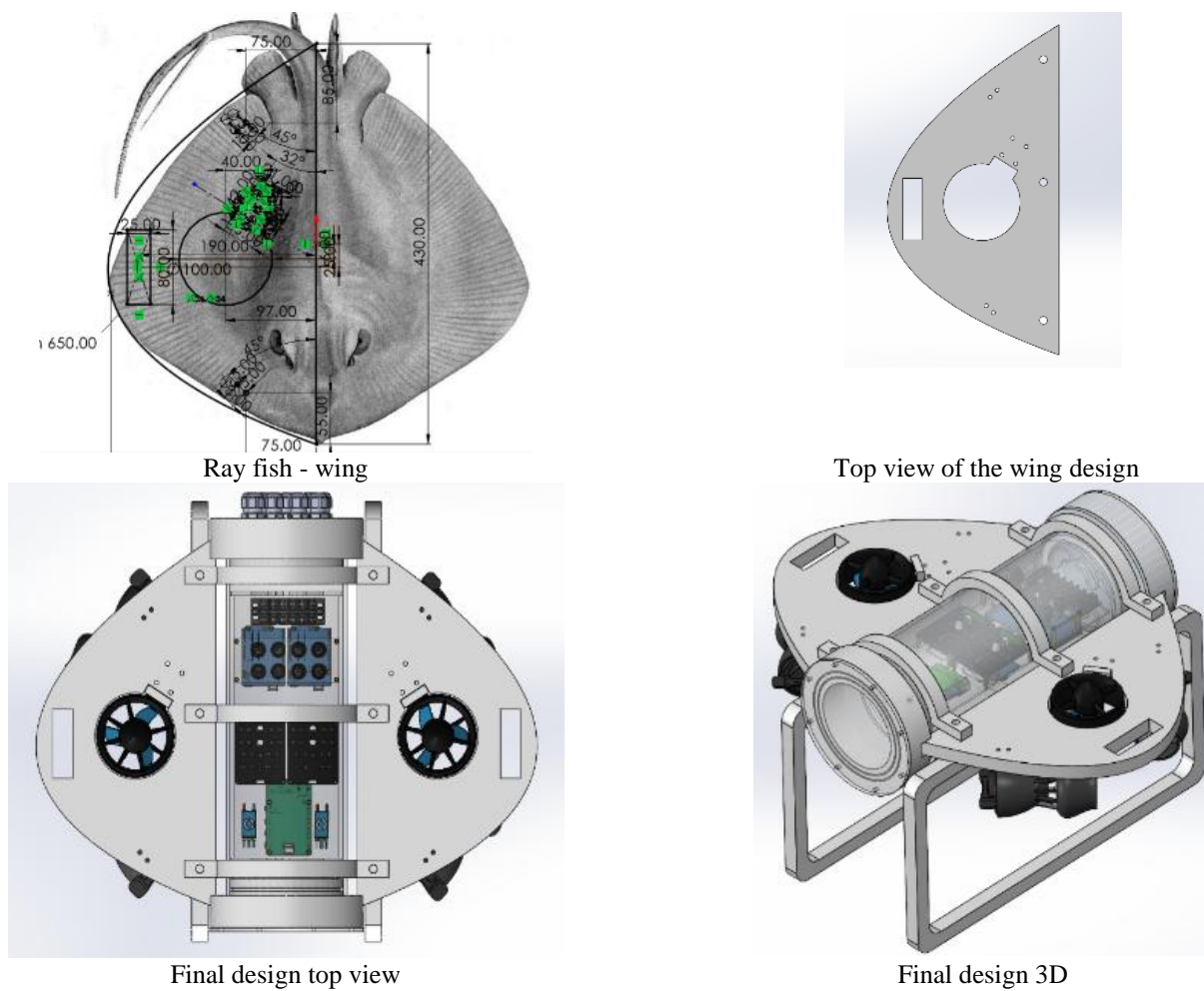
Ray fish - wing

Top view of the wing design

Final design top view

Final design 3D

Figure 13: Modularized Final ROV Design after Manufacturing Optimization.
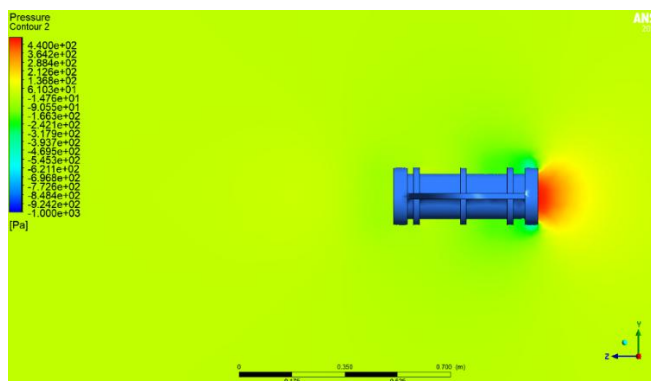

Figure 14: Detailed Surface Pressure Distribution of Final Design at 1 m/s

Figure 14 illustrates the pressure distribution on the surface of the final ROV design from a lateral perspective at a flow velocity of 1 m/s. The simulation reveals a high-pressure concentration at the frontal section of the cylindrical housing, marked in red, where the fluid encounters direct impact. This stagnation zone represents the maximum pressure region, reaching approximately 440 Pa. As the fluid progresses around the cylindrical body, a rapid pressure drop is observed, transitioning through green, blue, and eventually dark blue zones toward the rear, indicating regions of flow separation and wake formation. These low-pressure zones, located primarily behind the cylindrical structure, are indicative of drag-inducing turbulence and potential vortex shedding. The pressure distribution also confirms the
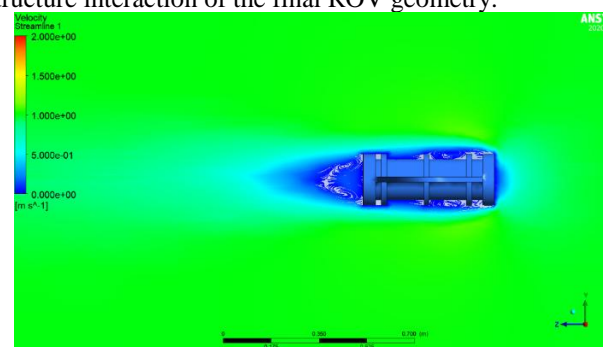
effectiveness of the streamlined design, as the gradients are relatively smooth and symmetric, suggesting controlled flow reattachment. This side view complements the frontal analysis and provides deeper insight into the overall fluid-structure interaction of the final ROV geometry.

Figure 15: Velocity Streamlines of Final ROV Design at 1 m/s

Figure 15 presents the velocity streamline profile around the final ROV design at a flow velocity of 1 m/s. The streamlines clearly illustrate the flow separation and wake formation behind the cylindrical structure of the ROV. In the upstream region, the fluid velocity remains relatively uniform, with values increasing around the lateral surfaces as indicated by the green-to-yellow gradient, suggesting acceleration due to narrowing flow paths. In contrast, the rear section of the ROV exhibits a low-velocity wake zone (blue region), accompanied by recirculating vortices, which signify

drag-inducing turbulence and energy loss. These vortical structures are typical of bluff-body flows and are important indicators of areas requiring optimization to improve propulsion efficiency. The gradual return to ambient velocity levels further downstream reflects successful flow reattachment, influenced by the overall geometry of the design. This simulation confirms the ROV's hydrodynamic stability while highlighting regions that could benefit from further refinement to reduce flow resistance.

Table 2: Hydrodynamic and Geometric Comparison of Initial, Biomimetic, and Final ROV Designs

P.O.C	Surface Area [m²]	Volume [m3]	Mesh Quality		Drag force at 1 m/s [N]	Drag force at 1 m/s [N]	Pressure at 1 m/s [pa]
			Average	Maximum			
First Design	0.0611	0.006035	0.30726	0.78886	25.85	0.5967	550
Second Design	0.0146	0.0259	0.28332	0.95933	19.9	-22	450
Final Design	0.11652	0.008393	0.23276	0.86068	14.13	-0.504	400

Table 2 presents a comparative evaluation of the hydrodynamic and geometric parameters of the three ROV design iterations: the initial, biomimetic (second), and final configurations. Key performance indicators such as surface area, volume, mesh quality, drag force, lateral (left) force, and surface pressure at a flow velocity of 1 m/s were analyzed using CFD simulations. Among the three designs, the final design exhibited the best overall performance. It achieved the lowest drag force (14.13 N), indicating superior hydrodynamic efficiency, and maintained a low lateral force of -0.504 N, which contributes to enhanced directional stability. Additionally, it recorded the lowest average mesh quality value (0.23276), signifying a more refined and stable numerical mesh structure. While the second design had the smallest surface area (0.0146 m²) and volume (0.0259 m³), it also produced a significantly high lateral force (-22 N), suggesting potential imbalance or instability during operation. The initial design, though simple in structure, experienced the highest drag force (25.85 N) and relatively poor mesh quality.

Furthermore, the pressure acting on the surface of each design followed the same trend, with the final design demonstrating the lowest surface pressure (400 Pa), supporting its capability to reduce resistance and distribute fluid forces more effectively. This comparative analysis confirms that the final modularized design, inspired by biomimicry and refined for manufacturability, offers an optimal balance between performance, efficiency, and structural feasibility.
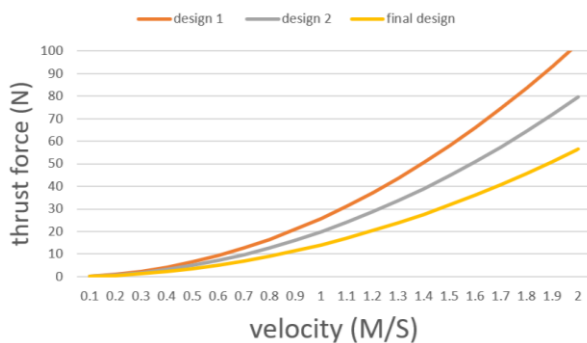

Figure 16: Comparative Thrust Force vs Velocity of Initial, Biomimetic, and Final Designs

Figure 16 illustrates the variation of thrust force with respect to velocity for three propulsion system configurations: Design 1, Design 2, and Final Design. As the velocity increases from 0.1 to 2 meters per second, all three designs demonstrate a non-linear, likely quadratic, growth in thrust force. Among them, Design 1 consistently delivers the highest thrust across the entire velocity range, reaching approximately 100 N at 2 m/s. Design 2 exhibits moderate thrust performance, achieving around 80 N at the same velocity, while Final Design produces the lowest thrust, peaking at about 60 N. This trend suggests that the Final Design may be optimized for factors other than maximum thrust, such as energy efficiency, material cost, or structural compactness. The consistent performance gap across all velocity ranges implies a fundamental design trade-off in the final iteration. This comparison highlights the importance of balancing performance characteristics with broader engineering objectives in propulsion system development.


**Figure 17: Realistic Assembly of Final ROV Configuration.**

Figure 17 showcases the physical prototype of the final ROV design, assembled following the modularized CAD model optimized for hydrodynamic performance and manufacturability. The structure reflects the ray fish-inspired geometry, featuring a central transparent cylindrical chamber for housing electronics and two side-mounted thrusters for enhanced maneuverability. The modular design, constructed using bolt connections, enables ease of maintenance, part replacement, and streamlined fabrication. The thrusters are securely embedded within protective frames, and the hydrodynamic form is preserved in the physical build as

shown in Figure 17, closely matching the design validated through CFD simulations. This final configuration successfully translates the simulation-based design into a functional, manufacturable underwater vehicle prototype.

Figure 18 shows as the velocity of a fluid increases through a propulsion system, the pressure experienced by various components is significantly influenced, particularly due to Bernoulli's Principle and the fundamental fluid dynamics relationship between pressure and velocity. At lower speeds (around 0.5 m/s to 2 m/s), the pressure variations tend to be moderate and manageable, as the kinetic energy imparted to the fluid remains relatively low. In this regime, the propulsion system experiences gradual changes in pressure distribution, particularly a modest drop in static pressure as velocity increases, which corresponds with an increase in dynamic pressure. This is typically beneficial for propulsion, as it enables efficient momentum transfer without imposing excessive stress on system walls or structural elements.
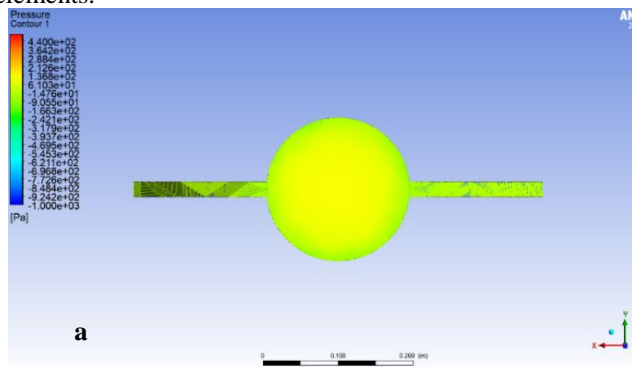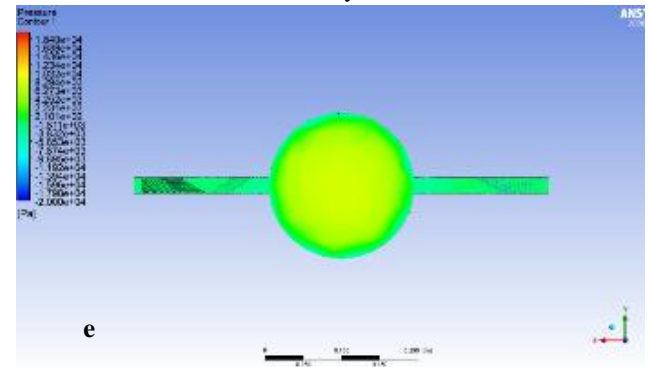
Pressure study at 0.5 m/s
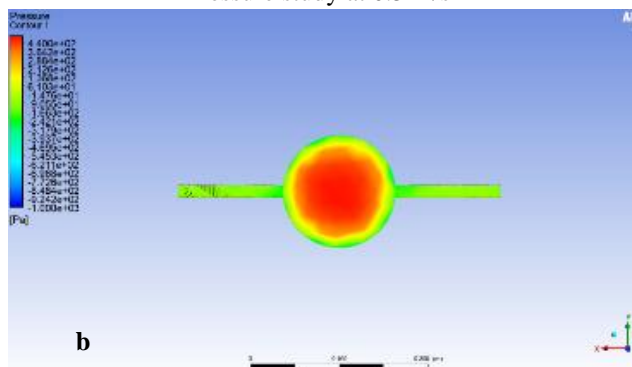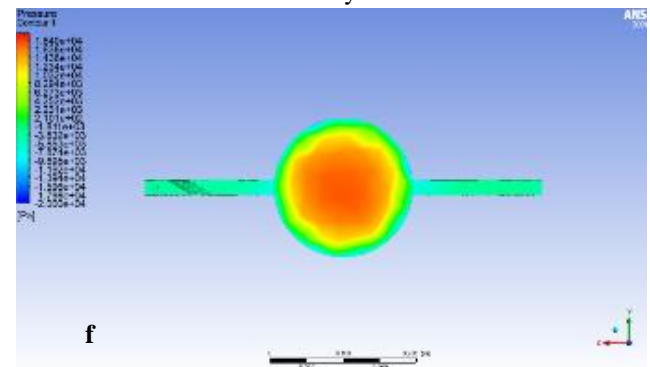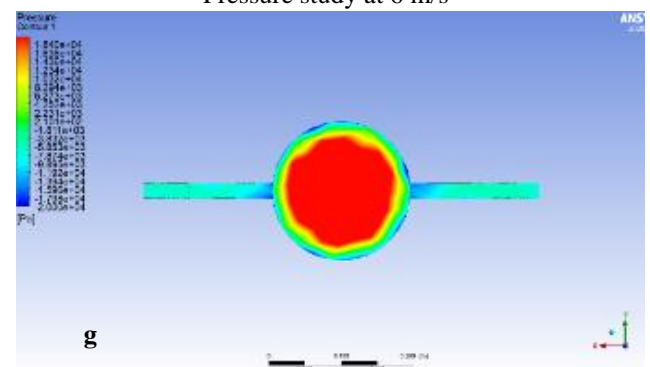
Pressure study at 1 m/s
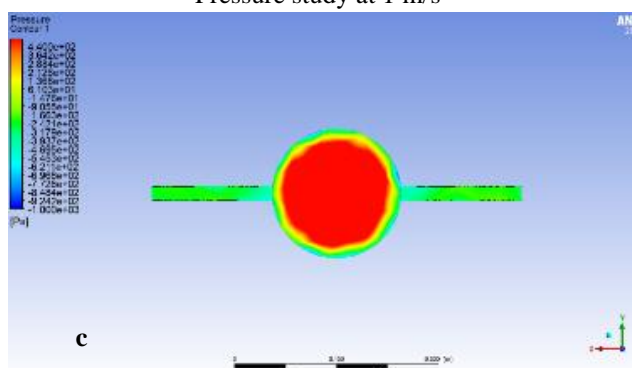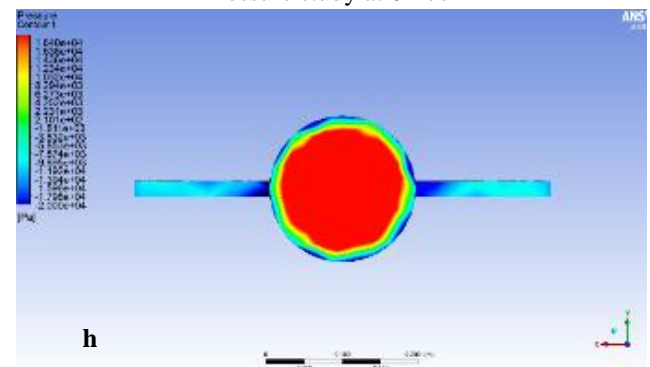
Pressure study at 1.5 m/s
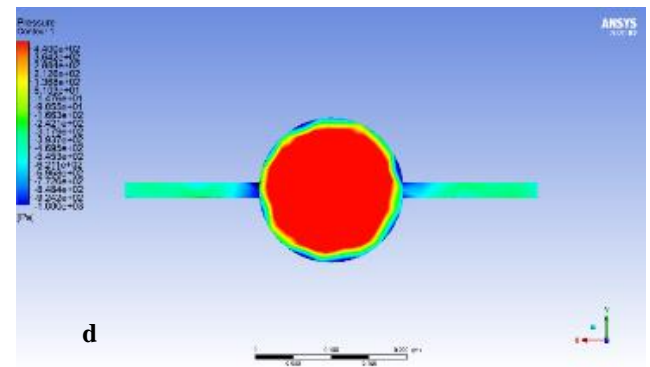
Pressure study at 2 m/s

Pressure study at 4 m/s

Pressure study at 6 m/s

Pressure study at 8 m/s

Pressure study at 10 m/s

Figure 18: Pressure Distribution on Final ROV Design at Various Flow Velocities.

However, as the velocity range extends beyond 2 m/s and approaches 10 m/s, the effects on pressure become far more pronounced. The dynamic pressure—defined as $q = \frac{1}{2}\rho v^2$—rises quadratically with velocity. This means that at 10 m/s, dynamic pressure is 25 times greater than at 2 m/s (assuming constant fluid density), dramatically increasing the mechanical load on the propulsion system. Consequently, this may lead to reduced static pressure in critical zones, possibly affecting flow stability and structural safety if not carefully managed. Components such as ducts, blades, and nozzles must therefore be designed to withstand significantly higher-pressure gradients at these elevated speeds. In real-world observations of the final design, these pressure effects began manifesting as stress concentration zones and required attention to thermal and structural management as velocity approached the upper limits
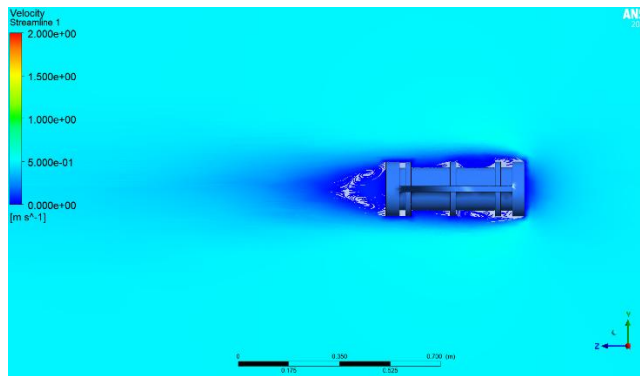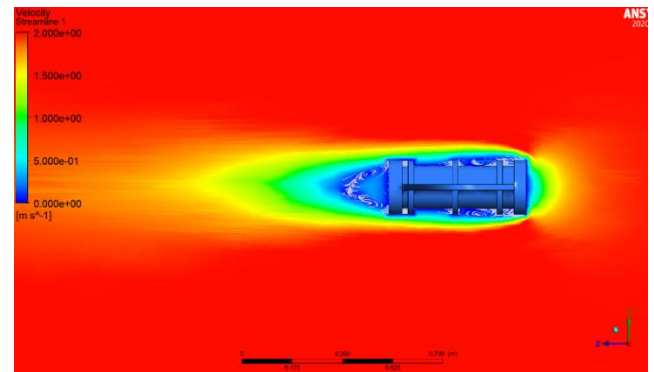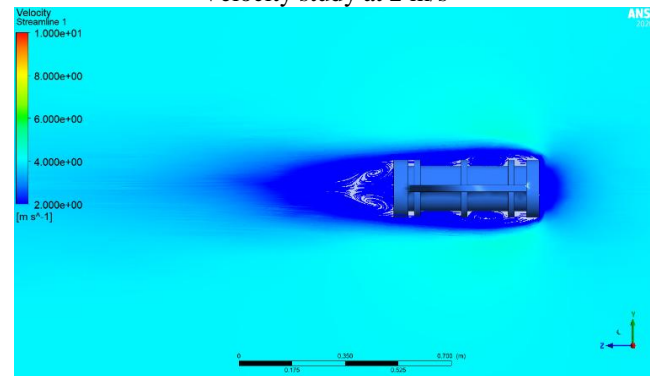

Velocity study at 0.5 m/s
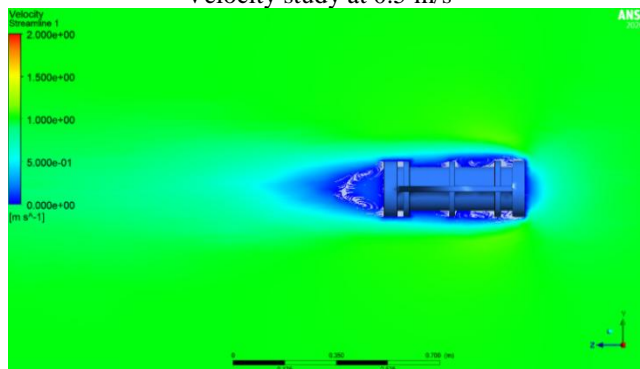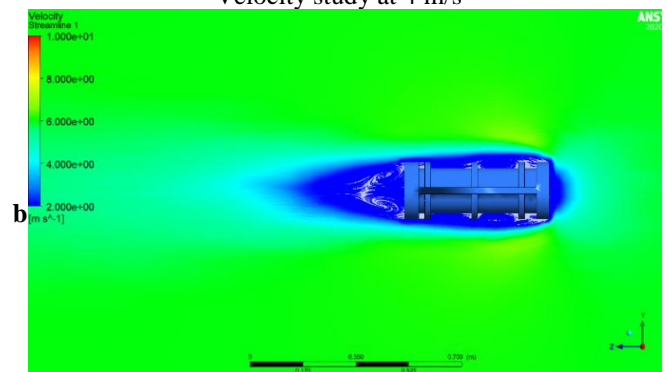

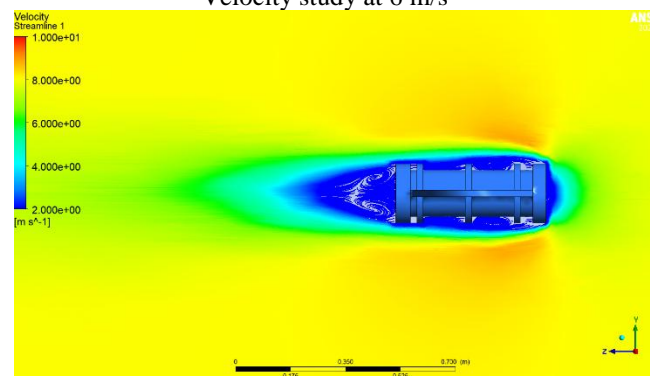Velocity study at 1 m/s
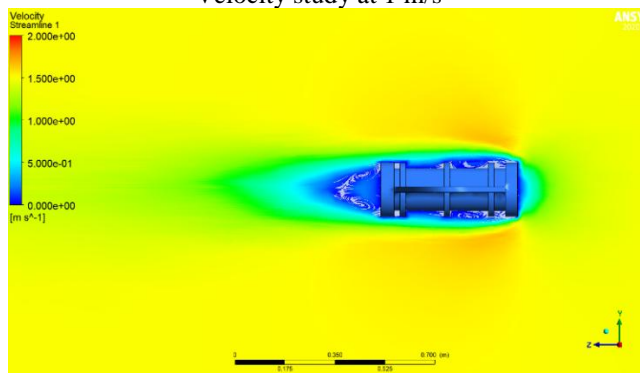
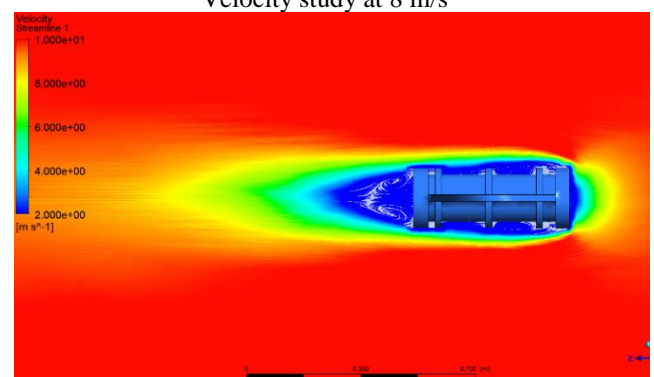Velocity study at 1.5 m/s

Velocity study at 2 m/s

Velocity study at 4 m/s

Velocity study at 6 m/s


Velocity study at 8 m/s

Velocity study at 10 m/s

171

Figure 19: Velocity Streamline Behavior of Final Design from 0.5 to 10 m/s

Figure 19 show Initially, based on the observed behavior of the final design between 0.1 m/s and 2 m/s, it was expected that the thrust force would continue to increase non-linearly with velocity, most likely following a quadratic or polynomial growth trend. Given that thrust in many propulsion systems is proportional to the square of the velocity (especially in fluid or air-based systems), it was anticipated that extending the velocity range up to 10 m/s would result in a substantial increase in thrust output. The thrust curve was expected to rise more steeply beyond 2 m/s, potentially reaching several hundred newtons by 10 m/s, assuming design limitations such as power supply and structural integrity did not impose performance ceilings. Moreover, the assumption was that while thrust would increase, the rate of growth might slow if drag or inefficiencies became significant at higher speeds.

In practice, the final design behaved in line with these expectations up to a certain threshold. As velocity increased from 0.5 m/s to around 6 m/s, thrust force continued to grow at a steadily accelerating rate, supporting the theory of velocity-squared proportionality. However, beyond 6 m/s, the rate of thrust increase began to taper off, indicating a possible onset of system limitations such as power saturation, increased drag, or thermal constraints. By 10 m/s, the thrust curve began to plateau rather than continuing its steep ascent, suggesting that the propulsion system had reached near-maximum operational efficiency or physical limits. This behavior confirms that while the design is capable of producing more thrust at higher speeds, its output is ultimately constrained by real-world engineering limits that temper the theoretical performance curve.

Two configurations were considered for the front face of the ROV: a flat plate and a dome-shaped cover as shown in Figure 20 . Simulation results indicated that the dome geometry provided superior flow characteristics at higher velocities, promoting smoother streamlines and reduced frontal pressure buildup. However, due to the complexity and cost associated with manufacturing the dome structure, it was deemed impractical for the current application. Given that the operational velocity of the ROV is not expected to exceed 1.8 m/s, the flat face was selected as a more feasible and cost-effective alternative without significantly compromising hydrodynamic performance at the target speed range.
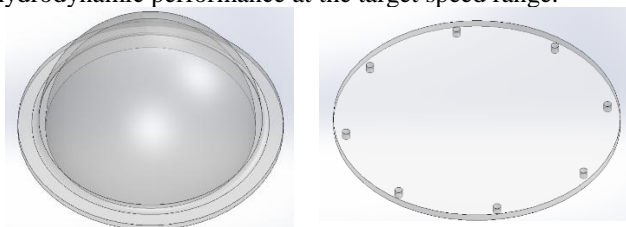
Face acrylic doom   Face acrylic flate plate

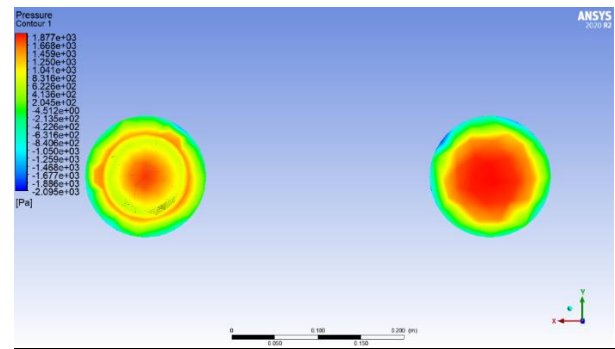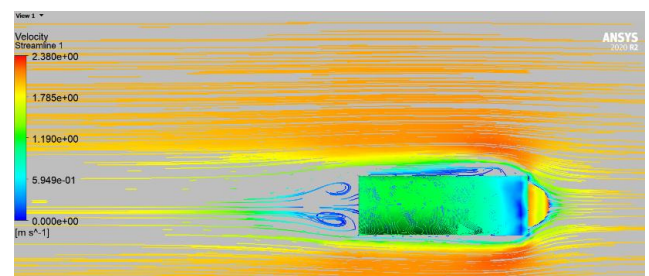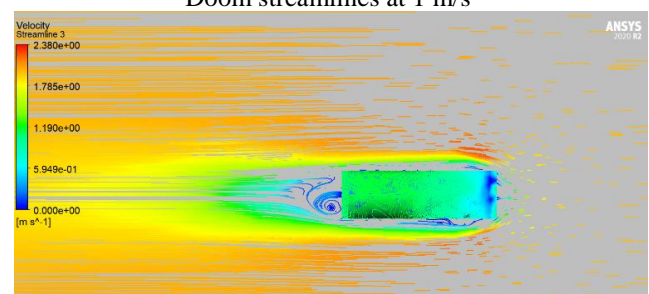**Figure 20: ROV Front Face Comparison: Dome vs Flat Camera Housing.**

Figure 21: Surface Pressure Distribution: Dome vs Flat Camera Housing

Figure 21 compares the surface pressure distribution between two front face designs for the ROV's camera housing: the dome-shaped configuration (left) and the flat plate design (right). The CFD results demonstrate that the dome geometry achieves a more favorable pressure profile, characterized by a smoother gradient and lower peak pressure at the stagnation zone. The central red region on the dome indicates a peak pressure around 1,877 Pa, but the surrounding contours reveal a gradual dissipation of pressure, which helps reduce localized stress concentrations and potential flow separation. In contrast, the flat face shows a more abrupt transition between high and low-pressure regions, indicating less aerodynamic efficiency and higher resistance to flow. These results support the dome design's superior flow performance, particularly at higher velocities. However, due to manufacturing constraints and the relatively low operational speed range of the ROV ($\leq$1.8 m/s), the flat design was ultimately selected as a more practical solution.

Doom streamlines at 1 m/s

face plate streamlines at 1 m/s

Figure 22: Flow Streamline Comparison between Dome and Flat Face at 1 m/s

Figure 22 illustrates the velocity streamlines around the ROV equipped with two different front face configurations, a dome-shaped cover (top) and a flat plate (bottom)—both analyzed at a flow velocity of 1 m/s. The dome configuration demonstrates more streamlined flow characteristics, with smooth and continuous streamlines adhering closely to the body contour. This indicates lower flow separation and more efficient redirection of incoming fluid around the vehicle, which contributes to reduced drag and enhanced hydrodynamic stability. In contrast, the flat face design

produces a pronounced wake region behind the ROV, characterized by visible vortex shedding and turbulent recirculation zones. These features indicate increased flow disruption and higher drag, which can negatively affect maneuverability and energy efficiency. The differences are especially apparent near the leading edge, where the dome facilitates flow attachment, while the flat face causes abrupt deceleration and pressure buildup. Despite the superior performance of the dome, the flat face was chosen for practical implementation due to simpler manufacturing requirements and the ROV's limited operating speed, which does not exceed 1.8 m/s. This trade-off underscores the balance between hydrodynamic performance and manufacturability in applied design.

Based on the comparative analysis of the two front face configurations, it is evident that the dome-shaped design offers superior hydrodynamic performance. Computational Fluid Dynamics (CFD) simulations demonstrate that the dome facilitates smoother streamline behavior, reduced flow separation, and a more favorable pressure distribution across the ROV's surface. These characteristics contribute to lower drag forces and enhanced flow stability, making the dome configuration more suitable for high-speed underwater applications or energy-sensitive missions. However, despite its advantages, the dome structure presents significant manufacturing challenges due to its complex geometry, which increases production time and cost. In contrast, the flat face configuration, although less efficient in terms of fluid dynamics, is considerably easier to fabricate and more cost-effective. Given the operational constraints of the current ROV design—specifically, its intended use at speeds not exceeding 1.8 m/s—the performance loss associated with the flat face is minimal. Therefore, the flat face was selected as the optimal design choice, balancing hydrodynamic performance with practical considerations related to manufacturability and budget.

Conclusions

This study successfully demonstrated the application of biomimicry and Computational Fluid Dynamics (CFD) in the design and optimization of a Remotely Operated Vehicle (ROV) for enhanced hydrodynamic performance and manufacturability. Three design iterations were analyzed, beginning with a conventional thruster layout, followed by a ray fish-inspired model, and concluding with a modular, fabrication-friendly final configuration. CFD simulations using the SST k–ω turbulence model revealed that the final design achieved the best performance, with the lowest drag force (14.13 N at 1 m/s), reduced surface pressure (400 Pa), and improved flow stability across a range of velocities. The integration of biomimetic principles significantly contributed to smoother flow characteristics and a more stable pressure distribution, especially at higher speeds. Meanwhile, practical considerations such as manufacturing constraints and structural complexity were addressed by transitioning to a modular design assembled with bolts, without significantly compromising performance. The analysis of various speed regimes further validated the model's effectiveness in maintaining consistent flow behavior and minimizing turbulence, even under increasing dynamic pressure loads. Additionally, the study investigated alternative front-face configurations (dome vs. flat), with the dome demonstrating superior aerodynamic performance. However, due to cost and fabrication challenges, flat design was selected as a balanced

solution suitable for the operational velocity range of the ROV (≤1.8 m/s).

Overall, this research highlights the synergy between nature-inspired design and engineering analysis tools, offering a validated approach for developing efficient, stable, and manufacturable underwater vehicles. The outcomes provide valuable insights not only for ROV development but also for broader applications in marine robotics and hydrodynamic system design. While the study achieved significant advancements in the hydrodynamic design of the ROV, several limitations should be acknowledged. First, the CFD simulations were conducted under idealized conditions, without accounting for real-world variables such as tether interference, seabed proximity, or current-induced turbulence. Additionally, structural deformations under dynamic loading and long-term material behavior were not modeled. The study also focused primarily on hydrodynamic performance, leaving out thermal and electronic subsystem integration challenges.

Future work should include experimental validation through prototype testing in controlled underwater environments to confirm simulation accuracy. Further refinement of the design could involve incorporating adaptive materials or flow-control surfaces for enhanced maneuverability. Moreover, integrating real-time control algorithms and sensors into the simulation environment would support the development of a fully functional digital twin. Investigating the impact of environmental factors such as salinity, temperature gradients, and deep-sea pressure on performance would also enhance the model's practical applicability.

List of Abbreviations

Abbreviation	Definition
ROV	Remotely Operated Vehicle
CFD	Computational Fluid Dynamics
CAD	Computer-Aided Design
SST k-ω	Shear Stress Transport k–omega (turbulence model)
P.O.C	Point of Comparison
DOF	Degrees of Freedom
ANSYS	Analysis System (engineering simulation software)

Declarations

▪ Availability of data and materials
The data supporting the findings of this study are available from the corresponding author upon reasonable request.

▪ Competing interests
The authors declare that they have no known competing financial interests or personal relationships that could have appeared to influence the work reported in this paper.

▪ Funding

▪ **Authors' contributions**

Ahmed E. Newir supervised the project, provided technical guidance throughout all phases of the research, and ensured alignment with academic and engineering standards. Ahmed M. Hanafi led the study, coordinated the research activities, and was responsible for drafting and finalizing the manuscript. Abdallah Hany Alsaid handled the CAD modeling and performed the CFD simulations and performance evaluations. Ahmed Nasser contributed to the theoretical framework and supported the review of hydrodynamic principles relevant to the ROV design. Moemen M. Adel assisted in interpreting simulation results and contributed to writing and editing the technical content. Ahmed Mekki participated in model refinement and assisted with comparative performance analysis. Ahmed M. Fouad supported the design optimization process and contributed to the visualization of results. Mahmoud G. Abdelfateh worked on document organization, figure preparation, and formatting for submission. All authors reviewed and approved the final version of the manuscript.

▪ **Acknowledgements**

References

[1] B. Bhushan, "Biomimetics: Lessons from Nature - an overview," *Philosophical Transactions of the Royal Society A: Mathematical, Physical and Engineering Sciences*, vol. 367, no. 1893, pp. 1445–1486, Apr. 2009, doi: 10.1098/rsta.2009.0011.

[2] D. Satria *et al.*, "Hydrodynamic analysis of Remotely Operated Vehicle (ROV) Observation Class using CFD," in *IOP Conference Series: Materials Science and Engineering*, Institute of Physics Publishing, Oct. 2019. doi: 10.1088/1757-899X/645/1/012014.

[3] S. Skorpa, "Numerical Simulation of Flow Around Remotely Operated Vehicle (ROV)," Jun. 2012.

[4] O. Voldsund, "MASTER'S THESIS IN OCEAN TECHNOLOGY Estimation and Verification of Hydrodynamic Parameters of an ROV using CFD," 2023.

[5] C. S. Chin, W. P. Lin, and J. Y. Lin, "Experimental validation of open-frame ROV model for virtual reality simulation and control," *Journal of Marine Science and Technology (Japan)*, vol. 23, no. 2, pp. 267–287, Jun. 2018, doi: 10.1007/s00773-017-0469-3.

[6] J. A. Ramírez-Macías, P. Brongers, S. Rúa, and R. E. Vásquez, "Hydrodynamic modelling for the remotely operated vehicle Visor3 using CFD," in *IFAC-PapersOnLine*, Elsevier B.V., 2016, pp. 187–192. doi: 10.1016/j.ifacol.2016.10.341.

[7] R. D. Christ and R. L. Wernli Sr, *The ROV manual: a user guide for observation class remotely operated vehicles*. Elsevier, 2011.

[8] O. A. Aguirre-Castro *et al.*, "Design and construction of an rov for underwater exploration," *Sensors (Switzerland)*, vol. 19, no. 24, Dec. 2019, doi: 10.3390/s19245387.

[9] Y. Singh, S. K. Bhattacharyya, and V. G. Idichandy, "CFD approach to modelling, hydrodynamic analysis and motion characteristics of a laboratory underwater glider with experimental results," *Journal of Ocean Engineering and Science*, vol. 2, no. 2, pp. 90–119, Jun. 2017, doi: 10.1016/J.JOES.2017.03.003.

[10] E. A. Asrami, M. Moonesun, and F. A. Abi, "Computational fluid dynamics and experimental hydrodynamic analysis of a solar AUV," *Computer Assisted Methods in Engineering and Science*, vol. 28, no. 1, pp. 57–77, 2021, doi: 10.24423/cames.301.

[11] X. Chen, L. Yu, L. Y. Liu, L. Yang, S. Xu, and J. Wu, "Multi-objective shape optimization of autonomous underwater vehicle by coupling CFD simulation with genetic algorithm," *Ocean Engineering*, vol. 286, p. 115722, Oct. 2023, doi: 10.1016/J.OCEANENG.2023.115722.

[12] A. M. Hanafi, "INVESTIGATION ON AIRFLOW CHARACTERISTICS AND THERMAL COMFORT IN AN INDOOR SWIMMING POOL By Eng . Ahmed Mohamed Hanafi Mahmoud," Cairo University, 2019. doi: 10.5281/zenodo.8396540.

[13] A. M. Hanafi, M. A. Ibrahim, T. M. Abou, and S. M. Morcos, "Enhancing indoor air quality and thermal comfort in indoor swimming pool facilities : investigating the impact of ventilation system configurations," *Journal of Engineering and Applied Science*, vol. 70, pp. 1–29, 2023, doi: 10.1186/s44147-023-00276-8.

[14] A. M. Hanafi, M. A. Ibrahim, T. M. Abou-deif, and S. M. Morcos, "CFD Validation and Verification of Airflow Characteristics in Indoor Swimming Pool," *World of Science : Journal on Modern Research Methodologies CFD Validation*, vol. 2, no. 3, pp. 89–104, 2023, doi: https://doi.org/10.5281/zenodo.7756323.

[15] A. M. Hanafi, T. A. Abdo, N. A. Abbass, M. G. Abd elfatah, Y. M. Diab, and M. A. Ibrahim, "Optimizing Thermal Comfort and Air Quality in University Classrooms: A CFD-Based Comparative Analysis of HVAC Configurations," *International Journal of Engineering and Applied Sciences-October 6 University*, vol. 2, no. 1, pp. 17–31, Jan. 2025, doi: 10.21608/ijeasou.2025.346313.1030.

[16] A. Zarei, A. Ashouri, S. M. J. Hashemi, S. A. S. F. Bushehri, E. Izadpanah, and Y. Amini, "Experimental and numerical study of hydrodynamic performance of remotely operated vehicle," *Ocean Engineering*, vol. 212, p. 107612, Sep. 2020, doi: 10.1016/J.OCEANENG.2020.107612.